

# Coherence in resonance fluorescence

Xu-Jie Wang,<sup>1</sup> Guoqi Huang,<sup>1,2</sup> Ming-Yang Li,<sup>3</sup> Yuan-Zhuo Wang,<sup>3</sup> Li Liu,<sup>1</sup> Bang Wu,<sup>1,\*</sup> Hanqing Liu,<sup>4,5</sup> Haiqiao Ni,<sup>4,5</sup> Zhichuan Niu,<sup>4,5</sup> Weijie Ji,<sup>1</sup> Rongzhen Jiao,<sup>2</sup> Hua-Lei Yin,<sup>1,3,6</sup> and Zhiliang Yuan<sup>1,†</sup>

<sup>1</sup>Beijing Academy of Quantum Information Sciences, Beijing 100193, China

<sup>2</sup>School of Science, Beijing University of Posts and Telecommunications, Beijing 100876, China

<sup>3</sup>National Laboratory of Solid State Microstructures and School of Physics,

Collaborative Innovation Center of Advanced Microstructures, Nanjing University, Nanjing 210093, China

<sup>4</sup>State Key Laboratory of Superlattices and Microstructures,  
Institute of Semiconductors, Chinese Academy of Sciences, Beijing 100083, China

<sup>5</sup>Center of Materials Science and Optoelectronics Engineering,  
University of Chinese Academy of Sciences, Beijing 100049, China

<sup>6</sup>Department of Physics and Beijing Key Laboratory of Opto-electronic Functional Materials and Micro-nano Devices,  
Key Laboratory of Quantum State Construction and Manipulation (Ministry of Education),  
Renmin University of China, Beijing 100872, China

(Dated: December 22, 2023)

**Resonance fluorescence (RF) serves as a fundamental path for matter to coherently interact with light. Accompanying this coherent process, recent studies suggested parallel existence of an incoherent scattering channel in order to explain the long-standing paradox of joint observation of a laser-like spectrum and anti-bunching in the RF of a weakly driven two-level emitter. If truly present, this incoherent process would cast doubt over RF's prospects in quantum information applications. Here, we exploit the concept of single-photon time-energy entanglement and have thus revolved the paradox without reliance on any incoherent scattering process. We derive a dimensionless dependence of the first-order coherence of the RF on the driving strength, followed by experimental verification on a cavity-enhanced quantum dot device with near-perfect light coupling. Furthermore, we perform the first phase-dependent two-photon interference experiment and observe peculiar coincidence bunching that is explained by single-photon time-energy entanglement. Our work reveals a new dimension in the understanding of photonic quantum superposition and may stimulate new applications.**

Resonance fluorescence (RF) has long been exploited for generating indistinguishable single photons<sup>1–6</sup>, creating time-bin photonic entanglement<sup>7–10</sup>, and exploring superradiant phenomena<sup>11,12</sup>. Yet, in its simplest form, paradox remains. RF of a two-level-emitter (TLE) under weak monochromatic excitation has been known for decades to display simultaneously anti-bunching in the photon number statistics and the driving laser's linewidth<sup>13–17</sup>. Anti-bunching implies photons were spontaneously emitted and must therefore possess a bandwidth no less than  $1/2\pi T_1$ , a limit imposed by the TLE's radiative lifetime  $T_1$ . A laser-like linewidth violates this limit.

The devil often hides in the detail. Lopez Carreno et al. insightfully looked into the so-called *incoherent* part in the RF, which can be vanishingly insignificant under weak excitation<sup>18</sup>, and identified theoretically that its interference with the dominant coherent signal can account for the anti-bunching<sup>19</sup>. Their theory immediately received experimental support that observed varying photon-number statistics after filtering through just the coherent<sup>20,21</sup> or incoherent<sup>22</sup> part of the RF. Albeit encouraging, these developments cannot resolve the para-

dox for two reasons. First, the theory<sup>19</sup> assumed existence of an incoherent scattering channel, but which lacks a concrete physical origin. Second, aggressive spectral filtering in experiments<sup>20–22</sup> elongates, and can thus cause overlap between, adjacent photon packets, the interference of which will create artifacts in the measured photon number statistics. Contrarily, these studies raise a pressing question of fundamental importance: Is there truly an *incoherent* scattering channel? An affirmative answer would profoundly change RF's prospects in quantum information processing.

Here, we dispel the myth of an incoherent scattering channel and resolve the subnatural linewidth paradox<sup>13,14,16</sup> by treating TLE's interaction with the light field a purely coherent process. We view the resulting RF as a stream of phase-locked lifetime-limited *broadband* single photons that are entangled in time-energy domain. It is the interference of these broadband photons, rather than two separate scattering mechanisms<sup>19</sup>, that gives rise to the sub-natural linewidth that is superimposed upon the so-called “incoherently scattered light”<sup>14,16,17,20,21</sup>. Moreover, we derive an explicit dependence of the first order coherence of the RF on the excitation power, which we successfully verify by experiments using a quantum dot (QD) micropillar device. Furthermore, we perform the first phase-dependent Hong-Ou-Mandel (HOM) two-photon interference<sup>23</sup> experiment, with its peculiar coincidence bunching successfully ex-

\* wubang@baqis.ac.cn

† yuanzl@baqis.ac.cn

plained by our model. Our work sheds new light into coherent light-matter interaction.

With reference to Fig. 1a, we explain the quantum state of the RF output. A monochromatic laser coherently drives a TLE, e.g., a QD in a micropillar cavity. We use  $\nu$ ,  $h\nu$  and  $T_L$  to depict the laser's frequency, photon energy and coherence time, respectively. Ignoring dephasing, the TLE will be coherently driven to oscillate between its ground state  $|g\rangle$  and excited state  $|e\rangle$  with full population swing at the Rabi frequency  $\Omega$  that is proportional to the driving field strength<sup>24</sup>. However, the excited state  $|e\rangle$  has a finite lifetime of  $T_1$ , and hence a maximum decoherence time of  $T_2 = 2T_1$ . Dephasing restricts the population swing amplitude and shortens the effective oscillation period to  $\sim 2T_2$ . To accommodate dephasing, we write the light-matter state as

$$|\psi\rangle = \sqrt{p_0}|0\rangle|g\rangle + \sqrt{p_1}e^{2i\pi\nu t}\left(\cos\frac{\omega t}{2}|0\rangle|e\rangle - i\sin\frac{\omega t}{2}|1\rangle|g\rangle\right), \quad (1)$$

where  $|0\rangle$  and  $|1\rangle$  are bare photon number states in the photonic subsystem,  $p_1$  represents the restricted population swing amplitude ( $p_0 + p_1 = 1$ ), and  $\omega \sim \pi/T_2$  the population swing angular frequency. Here,  $\omega$  should not be viewed as monochromatic, but instead as a broad distribution with its centre and width on the same order of magnitude,  $\Delta\omega \sim \langle\omega\rangle$ , that is determined by the TLE's coherent absorption and spontaneous emission processes. The amplitude  $p_1$  depends on the excitation intensity, and their exact relationship will be derived later. The form of  $|\psi\rangle$  implies two-fold entanglement. First, the light and matter are entangled in the basic state  $\cos\frac{\omega t}{2}|0\rangle|e\rangle - i\sin\frac{\omega t}{2}|1\rangle|g\rangle$ . Second, these basic entangled states are entangled again in time-energy domain because a fractional energy quanta, i.e.,  $p_1h\nu$ , does not exist alone.

Spontaneous emission decouples the matter and photonic sub-systems, radiating a photonic state

$$|\psi_{ph}\rangle = \sqrt{p_0}|0\rangle + \sqrt{p_1}e^{2i\pi\nu t}|1\rangle, \quad (2)$$

which is a single-photon time-energy entanglement. The overall radiation field is a coherent superposition of

temporally distributed phase-locked single-photon amplitude, or in other words, single-photon time-energy entanglement. Put simply, the RF signal is a multi-layered quantum mechanical superposition. At the lowest layer, all single photon states ( $|1\rangle$ ) are phase-locked by the driving laser. At the same time, their temporal amplitude distribution is restricted by the TLE, because a TLE emits one photon at a time and never two photons simultaneously. Furthermore, these photons inherit the property of  $|e\rangle \rightarrow |g\rangle$  transition of the TLE and have a natural linewidth of  $1/2\pi T_1$ . These properties guarantee observation of anti-bunching in the auto-correlation measurement. As shown below, interference of these phase-locked single photons recovers the laser-like linewidth in the spectral measurement.

The spectrum of the RF can be computed through Fourier transform of its first order correlation function  $g^{(1)}(\tau)$ . Since the RF field is time-invariant, it is legitimate to calculate  $g^{(1)}(\tau)$  using the basic photonic state  $|\psi_{ph}\rangle$  and we obtain for  $T_2 \ll \tau \ll T_L$ ,

$$g^{(1)}(\tau) = p_0 e^{-i2\pi\nu\tau}. \quad (3)$$

Here,  $|g^{(1)}(\tau)| = p_0$  represents the interference fringe visibility ( $V$ ) when the RF field couples its copy that is delayed by time  $\tau$  at a 50/50 beam splitter. Using Fourier transform, we can immediately deduce that the RF consists of a coherent, laser-like part that inherits the linewidth of the driving laser and has a spectral weight of  $I_{coh}/I_{tot} = p_0$ . The remaining spectrum will be of broadband in nature with a weight of  $I_{bb}/I_{tot} = 1 - p_0$ . We stress that the broadband part of the RF is also an interference outcome by the spectral measurement and cannot be literally viewed as incoherently scattered light. Prior to the measurement, all RF photons have a lifetime-limited bandwidth and phase locked by the driving laser. We give more discussion about  $g^{(1)}(\tau)$  and optical spectrum of RF in Supplementary Information Section I.

The non-unity coherence ( $p_0 < 1$ ) is caused by two-photon coalescence<sup>9</sup>, which becomes clearer if we write the tensor state for  $T_2 \ll \tau \ll T_L$  in the form

$$|\psi_{ph}(t)\rangle |\psi_{ph}(t+\tau)\rangle = p_0|0\rangle_t|0\rangle_{t+\tau} + \sqrt{p_0p_1}e^{i2\pi\nu t}(e^{i2\pi\nu\tau}|0\rangle_t|1\rangle_{t+\tau} + |1\rangle_t|0\rangle_{t+\tau}) + p_1e^{2i\pi\nu(2t+\tau)}|1\rangle_t|1\rangle_{t+\tau}. \quad (4)$$

When passing through an AMZI, the first term of the above state produces no observable effect as it contains no photons. The second term represents a photon that could arise from either an early photon  $|1\rangle_t$  passing through the AMZI's long arm or a late photon  $|1\rangle_{t+\tau}$  through the short arm with equal probabilities. These two probabilities are indistinguishable at the detector and thus produce measurable quantum mechanical interference, giving rise to the first-order coherence as outlined in

equation (3). The third term comprises two photons. When meeting at the exit beam splitter of the AMZI, they bunch together<sup>23</sup> and exit randomly from either output port, irrespective of the AMZI's phase delay. Consequently, this two-photon term reduces the overall interference fringe visibility. As bunching is a result of overlapping single photons, these bunched photons will exhibit a bandwidth governed by the TLE transition and thus contribute to the broadband part in the RF spec-

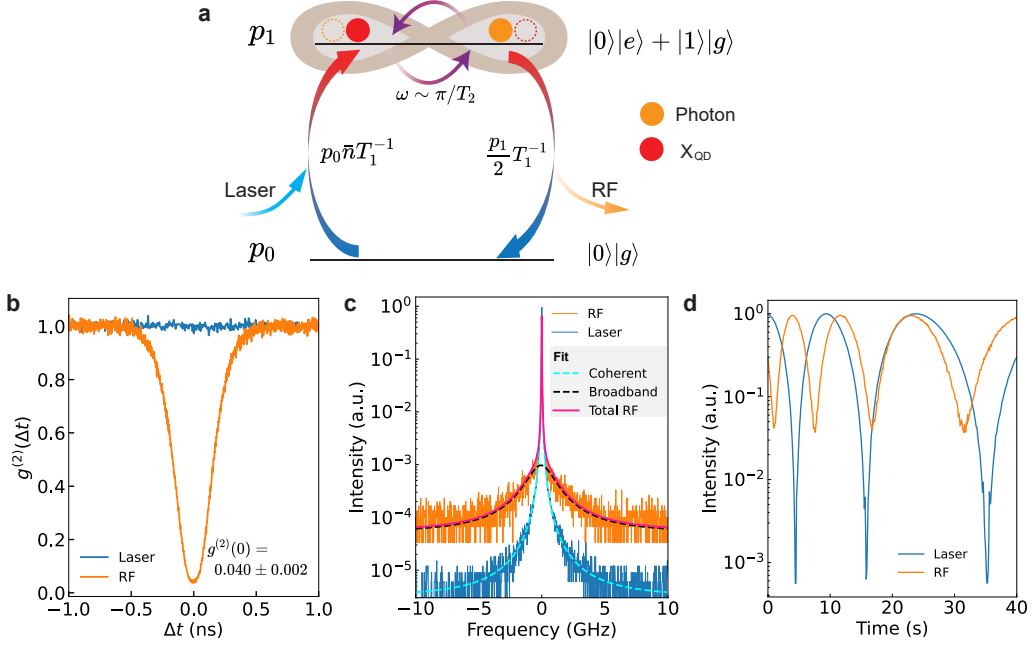


**Fig. 1 | Resonance fluorescence (RF).** **a**, Schematic for a two-level emitter (TLE) coherently driven by a continuous-wave laser. Here,  $|g\rangle$  and  $|e\rangle$  represent the bare ground and excited states of the TLE, while  $|0\rangle$  and  $|1\rangle$  the photon number states. Symbols  $T_1$ ,  $\bar{n}$ ,  $p_0$  and  $p_1$  represent the lifetime of the TLE's excited state ( $\text{QD}$  exciton,  $\text{X}_{\text{QD}}$ , in this case), the excitation photon flux per exciton lifetime, and populations of the system ground and excited states. The coherent driving field promotes the joint light-matter system into a superposition state as described in equation (1), with the excited state representing an oscillation between the matter and photonic sub-systems. The terms  $p_0 \bar{n} T_1^{-1}$  and  $\frac{p_1}{2} T_1^{-1}$  represent coherent absorption and spontaneous emission rates by the TLE, respectively. **b**, Second-order correlation function  $g^{(2)}(\Delta t)$  measurements. **c**, High resolution spectra. **d**, Interference fringes measured with an asymmetric Mach-Zehnder interferometer of 2.1 ns differential delay.

trum. Unsurprisingly, the broadband part of the RF itself will display photon bunching in the auto-correlation measurement, as Masters et al. observed recently<sup>22</sup>.

When the system reaches equilibrium, i.e., emission balances absorption, we have  $p_1/2T_1 = (1 - p_1)/T_1 \cdot \bar{n}$  (see Fig. 1a), leading to  $p_1 = 2\bar{n}/(1 + 2\bar{n})$ , where  $\bar{n}$  is the number of photons incident upon the TLE over  $T_1$  duration. In weak excitation limit, i.e.,  $\bar{n} \rightarrow 0$ , the population  $p_1 = 2\bar{n}$  equals to the number of photons incident over the TLE's dephasing time  $T_2$ , implying all incoming photons enter the light-matter state. Using  $I_{\text{coh}}/I_{\text{tot}} = 1 - p_1$ , we obtain a neat, dimensionless relation

$$I_{\text{coh}}/I_{\text{tot}} = \frac{1}{1 + 2\bar{n}}. \quad (5)$$

Despite its simple derivation, the result above is in excellent correlation with Mollow's elaborate theory<sup>18</sup>, which leads to  $I_{\text{coh}}/I_{\text{tot}} = 1/(1 + \Omega^2 T_1 T_2)$  in the absence of pure dephasing<sup>14</sup> ( $T_2 = 2T_1$ ). In fact, they become identical if we take  $\bar{n} = \Omega^2 T_1^2$ . This is not accidental. In weak excitation limit,  $2\Omega^2 T_1^2$  represents the  $|e\rangle$  population under the Rabi driving field of  $\Omega$  strength with  $T_2$  duration, just like  $p_1 = 2\bar{n}$  which we discussed earlier. Given that efficient light coupling was demonstrated with QD-

micropillar devices<sup>25</sup>, this presents a unique opportunity to test our model on RF's coherence, as we exercise below.

The QD sample we investigate contains a single InAs QD embedded in a micropillar cavity of 2.4  $\mu\text{m}$  in diameter and a quality factor ( $Q$ ) of 9350. It is kept in a closed-cycle cryostat and the QD's neutral exciton is temperature-tuned to resonate with the micropillar cavity at 15.2 K, emitting at 911.55 nm. We use a confocal microscope setup equipped with a tunable CW laser of 100 kHz linewidth as the excitation source and a 50/50 non-polarising beam splitter (NPBS) for routing the QD signal into measurement apparatuses. This NPBS configuration allows us to use any excitation polarisation and we choose to excite the vertically polarised exciton throughout this study unless specified otherwise. Without polarisation filtering, the RF signal is able to dominate over the laser background thanks to the ultra-low resonant cavity reflectivity of our micropillar device<sup>26</sup>. The setup allows characterisations of high-resolution spectroscopy, auto-correlation function  $g^{(2)}(\Delta t)$ , the first-order correlation function  $g^{(1)}(\tau)$ , and two-photon HOM interference. For detailed description of the experimental setup, see Supplementary Informa-

tion Section III.

The QD under investigation is characterised to have a Purcell enhanced lifetime of  $T_1 = 68.7$  ps, corresponding to a linewidth of  $\Gamma_{\parallel} = 2.32$  GHz. We use  $\bar{n}_{in} = P_{in}T_1/h\nu$ , i.e., which is strictly calibrated to represent the average number of photons incident upon the sample surface over  $T_1$  duration, to depict the excitation intensity. In the limit of 100 % light in-coupling,  $\bar{n}_{in} = \bar{n}$ . Based on the cavity resonance reflectivity of 0.015, we estimate the actual in-coupling efficiency greater than 98 %. More information about our QD-micropillar device is provided in Supplementary Information Section IV. In the first experiment, we use a weak excitation of  $\bar{n}_{in} = 0.0067$ , corresponding to a Rabi frequency of  $\Omega/2\pi = 196$  MHz ( $0.084\Gamma_{\parallel}$ ). Figure 1b shows the auto-correlation function  $g^{(2)}(\Delta t)$  for both the RF (orange line) and the laser (blue line). While the laser exhibits a flat  $g^{(2)}$  because of its Poissonian statistics, the RF exhibits a strong anti-bunching ( $g^{(2)}(0) = 0.040 \pm 0.002$ ) at 0-delay over a time-scale of  $\sim T_1$ , suggesting the QD scatters one photon at a time.

Figure 1c shows the RF frequency spectrum (orange line) measured with a scanning Fabry-Pérot interferometer (FPI). It is dominated by a sharp line that overlaps the laser spectrum (blue line) with a linewidth that is limited by the FPI resolution (20 MHz). The RF contains additionally a broadband pedestal whose amplitude is 3 orders of magnitude weaker. The overall spectrum can be excellently fit with two Lorentzians of 20 MHz and 2.2 GHz linewidths, shown as cyan and black dashed lines, respectively. The bandwidth of the latter closely matches the radiative linewidth of  $1/2\pi T_1$ . Following the discussion surrounding equation (4), we attribute the sharp and broadband features to the same origin, i.e., the interference outcome of the RF signal passing through the FPI. Coherent, laser-like fraction of the RF can be limited by both photon indistinguishability and  $|1\rangle$  state population.

Coherent fraction ( $I_{coh}/I_{tot}$ ) or the first-order interference visibility ( $V$ ) is best evaluated using an asymmetric Mach-Zehnder interferometer (AMZI) with its differential delay ( $\tau_0$ ) that meets  $T_2 \ll \tau_0 \ll T_L$ . Here, our AMZI has  $\tau_0 = 2.1$  ns and its build quality is confirmed by a fringe visibility of 0.999 measured with the laser (Fig. 1d). The RF's interference visibility drops noticeably to 0.92. We measure the power dependence of the interference visibility, with data summarised in Fig. 2. For  $\bar{n}_{in}$  up to 1, we observe a general trend of a decreasing coherent fraction as the excitation power increases. However, this drop should not be viewed as phase decoherence or photons becoming more distinguishable. Instead, it is caused by the increase of state  $|1\rangle$  population ( $p_1$ ) in the scattered time-energy entanglement, thereby leading to a poorer first-order interference visibility. For fluxes  $\bar{n}_{in} > 1.0$ , the coherent fraction reverses its downward trend and starts to climb up. In this regime, the RF signal starts to saturate<sup>26</sup> while the laser background continues to rise. Consequently, the laser-like (highly co-

herent) fraction in the QD output increases, which is supported by the accompanying sharp rise in  $g^{(2)}(0)$ .

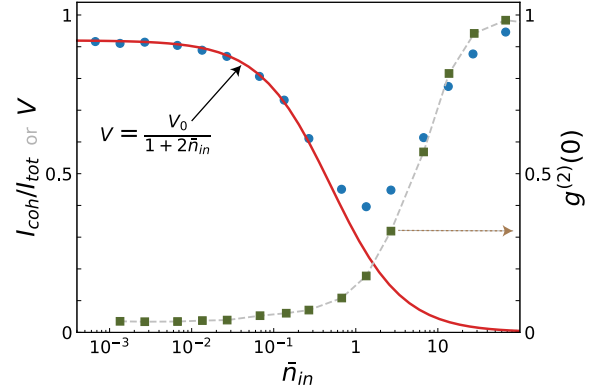


**Fig. 2 | Coherent fraction versus excitation power.** Visibility and coherent fraction in the total RF are equivalent:  $V = I_{coh}/I_{tot}$ . An AMZI of  $\tau_0 = 2.1$  ns delay was used in this measurement. Calculation (solid line) using  $V = V_0/(1 + 2\bar{n}_{in})$  reproduces experiment (solid circles) for  $\bar{n} < 0.3$  without the need for scaling  $\bar{n}_{in}$ . The discrepancy for  $\bar{n} > 0.3$  is attributed to an increased laser background, as evidenced by  $g^{(2)}(0)$  measurements (solid squares). Representative RF spectra are shown in Supplementary Information Section V.

According to equation (3),  $I_{coh}/I_{tot}$  should approach unity at weak excitation limit. However, the measured value plateaus at 0.92. This discrepancy is attributed to photon distinguishability, which could be caused by QD environmental charge fluctuation<sup>27</sup> as well as a small amount of laser background mixed into the RF. Taking the saturated value of  $V_0 = 0.92$ , we calculate the measured visibility using  $V = V_0/(1 + 2\bar{n}_{in})$  without the need for scaling the excitation intensity and achieve an excellent agreement with experiment for  $\bar{n}_{in} < 0.3$ , see Fig. 2. This success confirms both soundness of our simple model and a near-perfect incoming light coupling realized in our QD-micropillar device. In Supplementary Information Section V, we reaffirm this success with a different data set obtained with an RF setup that uses polarisation beam splitter for signal routing so that the RF is contaminated less by laser background.

We perform the first phase-dependent HOM two-photon interference experiment with the setup shown in Fig. 3a. As the AMZI drifts slowly, we are able to extract the phase information from the count-rate ratio of the two single-photon detectors during HOM interference and reconstruct phase-dependent correlation traces with phase intervals of  $\pi/20$ . We summarize the results in Figs. 3b–3d with observations: (1) The coincidence baseline is phase-dependent, but the gap between traces shrinks as the excitation power increases; (2) Strong anti-bunching at  $\Delta t = 0$  for all excitation intensities and phase values; (3) Features at  $\Delta t = \pm\tau_0$ , caused by the

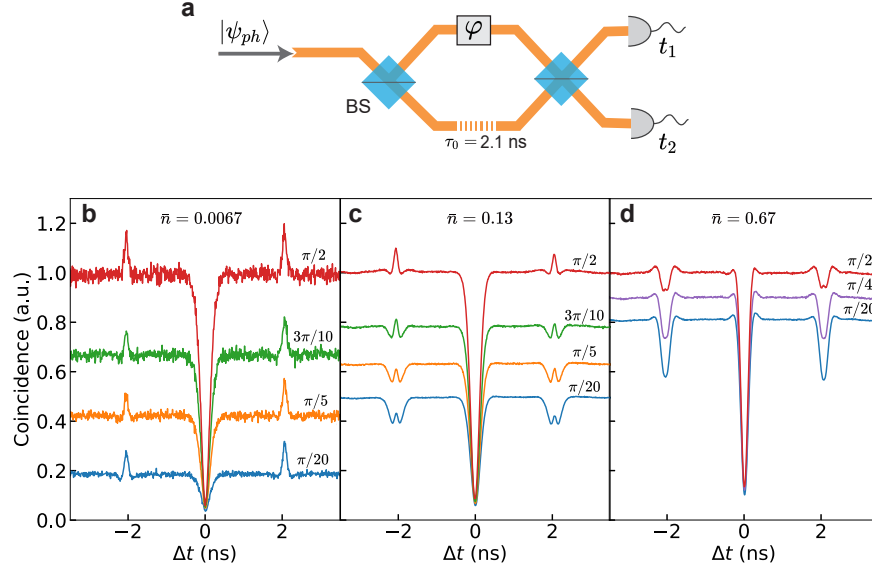


**Fig. 3 | Phase-dependent two-photon interference.** **a**, Asymmetric Mach-Zehnder interferometer with a differential delay of 2.1 ns. **b**, **c**, and **d**, Post-selected phase-dependent two-photon interference traces under three different excitation intensities.

AMZI's delay, can exhibit as peaks or dips depending on both the excitation power and the phase delay. We note that observation 3 is strikingly different from incoherently excited single-photon sources<sup>25,28</sup>, where the side features always display as dips with depth limited to

0.75.

To understand the HOM interferometric results, we derive in Supplementary Information Section II the theoretical coincidence probabilities and reproduce the main results below.

$$\mathcal{C}(0) = \frac{p_2}{4} (1 - p_0 M \cos 2\varphi) + \frac{p_1^2 + 4p_1 p_2 + 4p_2^2}{8} (1 - M), \quad (6A)$$

$$\mathcal{C}(\pm\tau_0) = \frac{p_1^2}{16} (3 - 2p_0 M \cos 2\varphi), \quad (6B)$$

$$\mathcal{C}_0 = \frac{p_1^2}{4} (1 - p_0^2 M \cos^2 \varphi), \quad (6C)$$

where  $M$  is the indistinguishability among single photon states,  $\mathcal{C}(\Delta t)$  represents the coincidence probability at time interval  $\Delta t$  while  $\mathcal{C}_0$  is the baseline coincidence for time intervals that meet the condition  $|\Delta t| \gg T_2$  and  $|\Delta t \pm \tau_0| \gg T_2$ . In the derivation of  $\mathcal{C}(0)$ , we use a time-energy entanglement state  $|\psi_{ph}\rangle = \sqrt{p_0}|0\rangle + \sqrt{p_1}|1\rangle + \sqrt{p_2}|2\rangle$  with a small two-photon probability  $p_2 \ll p_1^2/2$ , in order to account for the impact by the laser background. For other coincidences, we omit the state  $|2\rangle$  because of its negligible contribution. All coincidence probabilities are phase-dependent.  $\mathcal{C}_0$  and  $\mathcal{C}(\pm\tau_0)$ 's dependence arises from the first-order interference, while  $\mathcal{C}(0)$  contains non-negligible contribution from the interference between  $|2\rangle$

states at time delays differing by  $\tau_0$ . All coincidence probabilities reach their respective maxima at  $\varphi = \pi/2$ . Their oscillating amplitude shrinks with an increasing excitation power (lowering  $p_0$ ), which is in visible agreement with the experimental observation (Figs. 3b-3d) for the coincidence baseline as well as the features at  $\Delta t = \pm\tau_0$ .

To compare quantitatively, Fig. 4 plots the phase dependence of both the theoretical and experimental coincidence rates. We show just the result for  $\bar{n} = 0.13$  because this data set contains a crossover of  $\mathcal{C}(\pm\tau_0)$  across the coincidence baseline  $\mathcal{C}_0$ . We use maximum likelihood estimation method to determine a realistic set of parameters:  $p_0 = 0.760$ ,  $p_1 = 0.238$ ,  $p_2 = 1.12 \times 10^{-3}$  and  $M = 0.90$ , that provide the best fit to the data. As shown in Fig. 4,

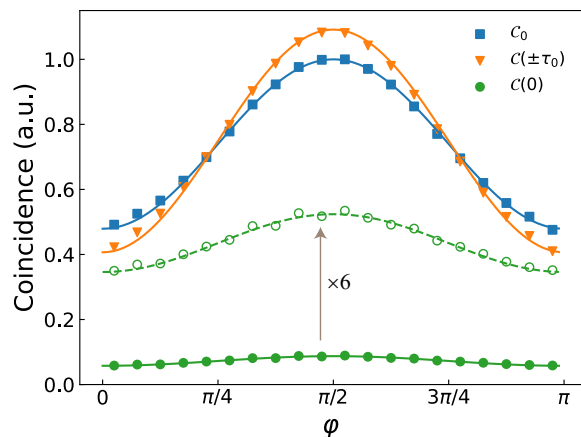


**Fig. 4 | Coincidence probabilities at  $\bar{n} = 0.13$ .** Solid symbols represent experimental data, where  $\mathcal{C}(\pm\tau_0) = \frac{1}{2}(\mathcal{C}(\tau_0) + \mathcal{C}(-\tau_0))$ . Solid lines are theoretical fittings using maximum likelihood estimation, based on equations (6A)  $\sim$  (6C). To better visualize the variation of  $\mathcal{C}(0)$  and assess the fit between the theoretical curve and the experimental data, we multiply the results of  $\mathcal{C}(0)$  on the y-axis by a factor of 6, as shown by the open circles and dashed line.

the theoretical simulations (solid lines) are in excellent agreement with the experimental data (symbols) for all coincidence rates and have also successfully reproduced the crossover between  $\mathcal{C}(\pm\tau_0)$  and  $\mathcal{C}_0$ . We conclude our theoretical model is sound.

Over past 50 years, it has been prevalent to discuss resonance fluorescence in the context of “coherently” and “incoherently” scattered light<sup>15,18–22</sup>. In literature, interchangeable terminologies, such as resonant Rayleigh scattering (RRS) vs. resonant photoluminescence (RPL)<sup>25</sup>

and elastic vs. inelastic scattering<sup>29</sup>, are also in use. The term “incoherent scattering” is not only confusing but has also severely misled at times. As we have elucidated, both coherent and broadband parts in the RF arise from the very same coherent scattering process, i.e., resonant absorption and spontaneous emission, that generates time-energy entanglement of phase-locked broadband single photons. The two parts are integral. Their integrity is key to the joint observation of “sub-natural” linewidth and antibunching. Conversely, any compromise in the integrity will inevitably change the photonic state and lead to different observations, e.g., loss of antibunching after spectral filtering<sup>20–22</sup>.

Our results have two immediate implications. First, it is *not* possible to exploit coherent scattering as a method to overcome dephasing mechanisms arising from material imperfection in solid-state systems, opposite to previously believed<sup>14,16,17</sup>. All single photons generated by RF underwent absorption and re-emission via the TLE, which thus had imprinted its property onto the scattered photons. Second, care needs to be taken in the evaluation of photon indistinguishability using an AMZI for RF-based single photon sources, because the relevant coincidences depend on the AMZI’s phase (see Fig. 4). We strongly recommend locking the AMZI’s phase to  $\pi/2$  for this evaluation, as we demonstrated in Supplementary Information Section V. This recommendation is relevant to pulsed excitation also, as it is hard to guarantee an exact  $\pi$ -pulse excitation condition that is required to ensure a minimal first-order interference.

The present work adds clarity to the knowledge pool of RF-based quantum light sources and we believe it will help foster new applications. One opportunity is to exploit the inherent time-energy single-photon entanglement for quantum secure communication<sup>30</sup>.

1. Carmichael, H. J. & Walls, D. F. Proposal for the measurement of the resonant stark effect by photon correlation techniques. *J. Phys. B At. Mol. Opt. Phys.* **9**, L43 (1976).
2. Kimble, H. J., Dagenais, M. & Mandel, L. Photon antibunching in resonance fluorescence. *Phys. Rev. Lett.* **39**, 691–695 (1977).
3. Lodahl, P., Mahmoodian, S. & Stobbe, S. Interfacing single photons and single quantum dots with photonic nanostructures. *Rev. Mod. Phys.* **87**, 347–400 (2015).
4. Somaschi, N. *et al.* Near-optimal single-photon sources in the solid state. *Nat. Photon.* **10**, 340 – 345 (2016).
5. Tömm, N. *et al.* A bright and fast source of coherent single photons. *Nat. Nanotech.* **16**, 399–403 (2021).
6. Lu, C.-Y. & Pan, J.-W. Quantum-dot single-photon sources for the quantum internet. *Nat. Nanotech.* **16**, 1294–1296 (2021).
7. Schwartz, I. *et al.* Deterministic generation of a cluster state of entangled photons. *Science* **354**, 434–437 (2016).
8. Peiris, M., Konthasinghe, K. & Müller, A. Franson interference generated by a two-level system. *Phys. Rev. Lett.* **118**, 030501 (2017).
9. Loredó, J. *et al.* Generation of non-classical light in a photon-number superposition. *Nat. Photon.* **13**, 803–808 (2019).
10. Appel, M. H. *et al.* Entangling a hole spin with a time-bin photon: a waveguide approach for quantum dot sources of multiphoton entanglement. *Phys. Rev. Lett.* **128**, 233602 (2022).
11. Lei, M. *et al.* Many-body cavity quantum electrodynamics with driven inhomogeneous emitters. *Nature* **617**, 271–276 (2023).
12. Tiranov, A. *et al.* Collective super- and subradiant dynamics between distant optical quantum emitters. *Science* **379**, 389–393 (2023).
13. Höffges, J., Baldauf, H., Eichler, T., Helmfrid, S. & Walther, H. Heterodyne measurement of the fluorescent radiation of a single trapped ion. *Opt. Commun.* **133**, 170–174 (1997).
14. Nguyen, H.-S. *et al.* Ultra-coherent single photon source.

- Appl. Phys. Lett.* **99**, 261904 (2011).
15. Konthasinghe, K. *et al.* Coherent versus incoherent light scattering from a quantum dot. *Phys. Rev. B* **85**, 235315 (2012).
  16. Matthiesen, C., Vamivakas, A. N. & Atatüre, M. Subnatural linewidth single photons from a quantum dot. *Phys. Rev. Lett.* **108**, 093602 (2012).
  17. Matthiesen, C. *et al.* Phase-locked indistinguishable photons with synthesized waveforms from a solid-state source. *Nat. Commun.* **4**, 1600 (2013).
  18. Mollow, B. R. Power spectrum of light scattered by two-level systems. *Phys. Rev.* **188**, 1969–1975 (1969).
  19. López Carreño, J. C., Zubizarreta Casalengua, E., Laussy, F. P. & del Valle, E. Joint subnatural-linewidth and single-photon emission from resonance fluorescence. *Quant. Sci. Technol.* **3**, 045001 (2018).
  20. Phillips, C. L. *et al.* Photon statistics of filtered resonance fluorescence. *Phys. Rev. Lett.* **125**, 043603 (2020).
  21. Hanschke, L. *et al.* Origin of antibunching in resonance fluorescence. *Phys. Rev. Lett.* **125**, 170402 (2020).
  22. Masters, L. *et al.* On the simultaneous scattering of two photons by a single two-level atom. *Nat. Photon.* **17**, 972–976 (2023).
  23. Hong, C. K., Ou, Z. Y. & Mandel, L. Measurement of subpicosecond time intervals between two photons by interference. *Phys. Rev. Lett.* **59**, 2044–2046 (1987).
  24. Steck, D. A. Quantum and atom optics. <http://steck.us/teaching> (revision 0.14, 23 August 2023).
  25. Proux, R. *et al.* Measuring the photon coalescence time window in the continuous-wave regime for resonantly driven semiconductor quantum dots. *Phys. Rev. Lett.* **114**, 067401 (2015).
  26. Wu, B. *et al.* Mollow triplets under few-photon excitation. *Optica* **10**, 1118 – 1123 (2023).
  27. Zhai, L. *et al.* Low-noise GaAs quantum dots for quantum photonics. *Nat. Commun.* **11**, 4745 (2020).
  28. Patel, R. B. *et al.* Postselective two-photon interference from a continuous nonclassical stream of photons emitted by a quantum dot. *Phys. Rev. Lett.* **100**, 207405 (2008).
  29. Metcalfe, M., Solomon, G. S. & Lawall, J. Heterodyne measurement of resonant elastic scattering from epitaxial quantum dots. *Appl. Phys. Lett.* **102**, 231114 (2013).
  30. Zhou, L. *et al.* Experimental quantum communication overcomes the rate-loss limit without optical phase tracking. *Phys. Rev. Lett.* **130**, 250801 (2023).

### Data availability

All the data that support the plots within this manuscript and other findings of this study are available from the corresponding authors upon reasonable request.

### Acknowledgements

Z.Y. acknowledges helpful discussions with Z. Q. Yin, Y. K. Wu, Y. Ji and X. B. Wang. This work was supported by the National Natural Science Foundation of China under grants 12204049 (X.-J.W.) and 62250710162 (Z.Y.), National Key R & D Program of China under grant 2018YFA0306101 (Z.N.), and Beijing Natural Science Foundation under grant IS23011 (Z.Y.).

### Author contributions

Z.Y., X.-J.W. and B.W. designed the research and experiments. X.-J.W., G.H. and B.W. carried out the experiments. M.-Y.L., Y.-Z.W., H.-L.Y. and X.-J.W. developed the theoretical model on phase-dependent two-photon interference and performed the simulations. L.L. fabricated the devices with assistance from W.J. H.L., H.N. and Z.N. grew the semiconductor wafer. X.-J.W. and Z.Y. wrote the paper with input from all authors. Z.Y. supervised the project.

### Competing interests

The authors declare no competing interests.



# Supplementary Information for “Coherence in Resonance Fluorescence”

Xu-Jie Wang,<sup>1</sup> Guoqi Huang,<sup>1,2</sup> Ming-Yang Li,<sup>3</sup> Yuan-Zhuo Wang,<sup>3</sup> Li Liu,<sup>1</sup> Bang Wu,<sup>1,\*</sup> Hanqing Liu,<sup>4,5</sup> Haiqiao Ni,<sup>4,5</sup> Zhichuan Niu,<sup>4,5</sup> Weijie Ji,<sup>1</sup> Rongzhen Jiao,<sup>2</sup> Hua-Lei Yin,<sup>1,3,6</sup> and Zhiliang Yuan<sup>1,†</sup>

<sup>1</sup>*Beijing Academy of Quantum Information Sciences, Beijing 100193, China*

<sup>2</sup>*School of Science, Beijing University of Posts and Telecommunications, Beijing 100876, China*

<sup>3</sup>*National Laboratory of Solid State Microstructures and School of Physics, Collaborative Innovation Center of Advanced Microstructures, Nanjing University, Nanjing 210093, China*

<sup>4</sup>*State Key Laboratory of Superlattices and Microstructures, Institute of Semiconductors, Chinese Academy of Sciences, Beijing 100083, China*

<sup>5</sup>*Center of Materials Science and Optoelectronics Engineering, University of Chinese Academy of Sciences, Beijing 100049, China*

<sup>6</sup>*Department of Physics and Beijing Key Laboratory of Opto-electronic Functional Materials and Micro-nano Devices, Key Laboratory of Quantum State Construction and Manipulation (Ministry of Education), Renmin University of China, Beijing 100872, China*

## I. THE FIRST-ORDER CORRELATION FUNCTION $g^{(1)}(\tau)$ AND OPTICAL FREQUENCY SPECTRUM OF RESONANCE FLUORESCENCE

The first-order correlation function  $g^{(1)}(\tau)$  is useful to characterise the coherence of an optical field<sup>1</sup>. It measures the normalised interference outcome of an optical field with its delayed copy by time  $\tau$ ,

$$g^{(1)}(\tau) = \frac{\langle \hat{E}^{(-)}(t) \hat{E}^{(+)}(t + \tau) \rangle}{\langle \hat{E}^{(-)}(t) \hat{E}^{(+)}(t) \rangle}, \quad (\text{S.1})$$

where  $\hat{E}^{(+)}(t) = E_0 a(t)$  and  $\hat{E}^{(-)}(t) = E_0 a^\dagger(t)$  with  $a(t)$  and  $a^\dagger(t)$  being photon annihilation and creation operators and  $E_0$  the electric field per photon. Its absolute value represents the interference visibility:  $V = |g^{(1)}(\tau)|$ . Experimentally,  $|g^{(1)}(\tau)|$  is measurable with a Mach-Zehnder (or Michaelson) interferometer that is equipped with a variable delay line, as schematically shown in Supplementary Fig. 1a.

Classically, a light source is said to be incoherent if  $|g^{(1)}(\tau)| = 0$  and coherent if  $|g^{(1)}(\tau)| = 1$  for  $\tau \neq 0$ . For example, a monochromatic light is perfectly coherent as  $|g^{(1)}(\tau)| \equiv 1$ . With knowledge of its  $g^{(1)}(\tau)$ , it is straightforward to calculate the frequency spectrum of a light source using Wiener-Khinchin theorem,

$$I(\nu) = \int_0^\infty g^{(1)}(\tau) e^{i2\pi\nu\tau} d\tau, \quad (\text{S.2})$$

where  $\nu$  denotes optical frequency. A coherent source has a  $\delta$ -function like spectrum.

Care needs to be taken when applying the above terminology to a quantum light source. Consider an ideal, deterministic single photon source realised with a two-level-emitter (TLE) under strict  $\pi$ -pulse resonant excita-

tion<sup>2</sup>. All single photons it emits are indistinguishable and synchronised in phase. In this sense, such source is perfectly coherent. Yet, using equation (S.1), we will obtain  $|g^{(1)}(\tau)| = 0$  for all  $\tau \gg T_2$ , where  $T_2$  is the TLE's dephasing time. This is because of two-photon interference, i.e., two indistinguishable photons meeting at a 50/50 beam splitter will coalesce and exit randomly from one of the exiting ports. In order not to confuse, we avoid use of the term “incoherent” in describing resonance fluorescence (RF) and instead adopt the term “broadband” to describe the part of the emission that does not produce first-order interference fringes. We continue to use the word “coherent” to describe the spectrally narrow part of the RF.

We now derive the first-order correlation function for RF of a TLE driven by a continuous-wave laser with a coherence time of  $T_L$ . Here, we start with an ideal scenario, i.e., the excitation laser is in perfect coupling with the emitter that is free from pure dephasing, and the RF signal is free of laser background. We write the RF's photonic state as

$$|\psi_{ph}(t)\rangle = \sqrt{p_0}|0\rangle_t + \sqrt{p_1}e^{2i\pi\nu t}|1\rangle_t, \quad (\text{S.3})$$

where  $|0\rangle_t$  denotes vacuum state while  $|1\rangle_t$  represents a single photon state emitted at time  $t$ . As derived in Main Text, the coefficients  $p_0$  and  $p_1$  have the following form,

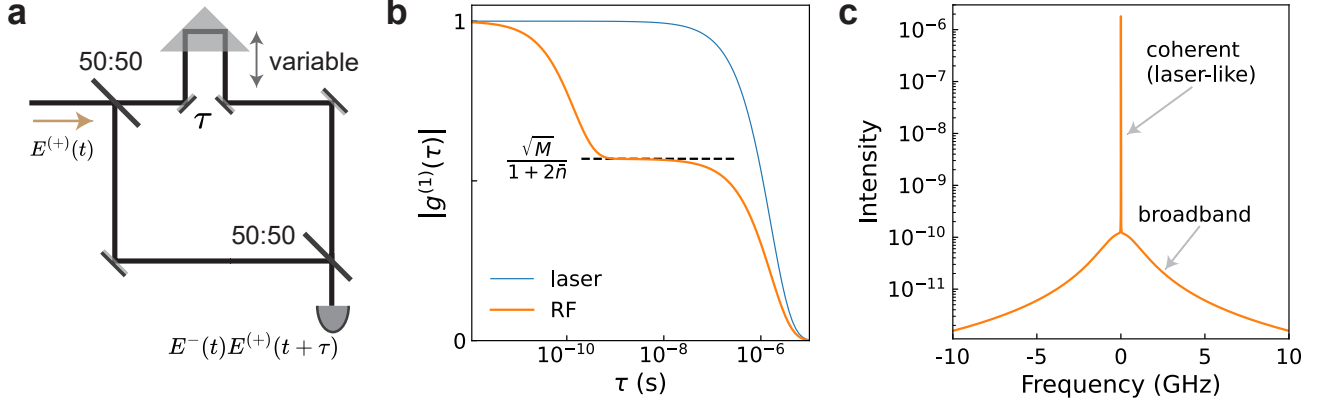
$$\begin{aligned} p_0 &= 1/(1 + 2\bar{n}), \\ p_1 &= 2\bar{n}/(1 + 2\bar{n}), \end{aligned} \quad (\text{S.4})$$

where  $\bar{n}$  represents the excitation intensity and is defined as the incident photon number over the duration of the TLE's spontaneous lifetime. For  $T_2 \ll \tau \ll T_L$ , we obtain

\* wubang@baqis.ac.cn

† yuanzl@baqis.ac.cn





**Supplementary Fig. 1. The first-order coherence function and optical frequency spectrum.** **a**, An experimental schematic diagram that can be used to measure first-order correlation  $g^{(1)}(\tau)$  as a function of a variable time delay  $\tau$ . **b**, Theoretical  $g^{(1)}(\tau)$  of RF under relatively low excitation power as a function of delay  $\tau$ . The curve reveals that the decay of  $|g^{(1)}(\tau)|$  exhibits two characteristic times: one is related to the TLE's dephasing time  $T_2$  and another is related to the laser coherence time  $T_L$ . As a comparison, we also provide the theoretical  $|g^{(1)}(\tau)|$  of the laser. **c**, RF spectrum obtained by performing Fourier transform on the first-order correlation function  $|g^{(1)}(\tau)|$  shown in panel **b**. The coherent component of the spectrum corresponds to the slowly decaying portion in  $|g^{(1)}(\tau)|$ , while the broadband corresponds to the rapidly decaying portion of  $|g^{(1)}(\tau)|$ . In the calculation, we use  $T_2 = 137.4$  ps and  $T_L = 1.59$   $\mu$ s, corresponding to our experimental parameters of QD's lifetime of 68.7 ps and the laser's linewidth of 100 kHz.

$$g_{RF}^{(1)}(\tau) = \frac{\langle \psi_{ph}(t) | \langle \psi_{ph}(t+\tau) | a^\dagger(t+\tau)a(t) | \psi_{ph}(t) \rangle | \psi_{ph}(t+\tau) \rangle}{\langle \psi_{ph}(t) | \langle \psi_{ph}(t+\tau) | a^\dagger(t)a(t) | \psi_{ph}(t) \rangle | \psi_{ph}(t+\tau) \rangle} e^{-2i\pi\nu\tau} = \frac{1}{1+2\bar{n}} e^{-2i\pi\nu\tau}, \quad (\text{S.5})$$

where

$$|\psi_{ph}(t)\rangle |\psi_{ph}(t+\tau)\rangle = p_0|0\rangle_t|0\rangle_{t+\tau} + \sqrt{p_0p_1}e^{i2\pi\nu t}(e^{i2\pi\nu\tau}|0\rangle_t|1\rangle_{t+\tau} + |1\rangle_t|0\rangle_{t+\tau}) + p_1e^{2i\pi\nu(2t+\tau)}|1\rangle_t|1\rangle_{t+\tau}. \quad (\text{S.6})$$

It is immediately apparent that  $|g_{RF}^{(1)}(\tau)| = 1/(1+2\bar{n}) < 1$  and the coherence decreases monotonically as the excitation intensity increases. The first-order coherence arises from quantum interference between two probability amplitudes of a photon emitted at  $t$  and  $t+\tau$ , as implied by the second term in equation (S.6),  $e^{i2\pi\nu\tau}|0\rangle_t|1\rangle_{t+\tau} + |1\rangle_t|0\rangle_{t+\tau}$ . The drop of  $|g_{RF}^{(1)}(\tau)|$  from unity is caused by two-photon interference, as shown by the third term in equation (S.6),  $|1\rangle_t|1\rangle_{t+\tau}$ . It contains two photons, one emitted at  $t$  and the other at  $t+\tau$ . When these photons meet at a 50/50 beam splitter, they coalesce together and exit from one of the exiting ports together independent of their mutual phase. Naturally, the stronger the excitation, the more likely the more frequent the two-photon events and thus the poorer the first-order coherence.

The discussion above is based on the assumption that single photons emitted by the TLE are perfectly indistinguishable. However, photons scattered out by the TLE underwent coherent absorption and spontaneous emission processes, and therefore their indistinguishability was degraded by the TLE's dephasing processes that are inherent in solid-state quantum systems as experimentally investigated in this study. Taking into account

of dephasing-induced distinguishability as well as mixed-in laser background, the first order coherence is revised accordingly to<sup>3</sup>

$$|g_{RF}^{(1)}(\tau)| = \frac{\sqrt{M}}{1+2\bar{n}}. \quad (\text{S.7})$$

This equation allows two novel measurements for photon indistinguishability  $M$  and how well the incoming light coupling into the cavity. The former can be measured as  $M = |g_{RF}^{(1)}(\tau)|^2$  under weak excitation limit, while the latter is extractable through how soon and how fast  $|g_{RF}^{(1)}(\tau)|$  decreases with the excitation intensity.

For short delays, i.e.,  $\tau \in [0, T_2]$ , the first-order correlation function measures the interference of an RF photon with itself. Therefore, the decay of  $|g_{RF}^{(1)}(\tau)|$  is governed by the TLE's dephasing time  $T_2$  alone under weak excitation, and will become mediated by the Rabi oscillation under strong excitation. The short decay will reach a visibility plateau that is determined by both photon indistinguishability ( $M$ ) and the excitation intensity ( $\bar{n}$ ), as illustrated by a theoretical simulation in Supplementary Fig. S.7b.

Through Fourier transform, we can calculate the RF frequency spectrum as shown in Supplementary Fig. 1c. Closely resembling the experimental data presented in Fig. 1c, Main Text, the spectrum contains a coherent part that inherits the laser linewidth and a broadband part with the TLE's bandwidth. The spectral weight of the coherent part,  $I_{coh}/I_{tot}$ , equals to the plateau  $|g^{(1)}(\tau)|$  value shown in Supplementary Fig. 1b. When applying spectral filtering to separate these two parts, the coherent part will behave like a coherent signal and exhibit a  $g^{(2)} = 1$  as experimentally demonstrated<sup>4,5</sup>. The broadband part is slightly more complicated. According to equation (S.6), it has contributions from both poor single-photon interference due to photon distinguishability and two-photon interference. The relative weight between these contributions depends on photon indistinguishability and excitation intensity. In the limit of perfect indistinguishability, the broadband part will contain only photon pairs. We believe the observation of photon bunching by Masters et al.<sup>6</sup> is a result of two-photon interference, rather than the TLE's simultaneous scattering of two photons suggested by the authors.

## II. PHASE-DEPENDENT HONG-OU-MANDEL INTERFEROMETRY

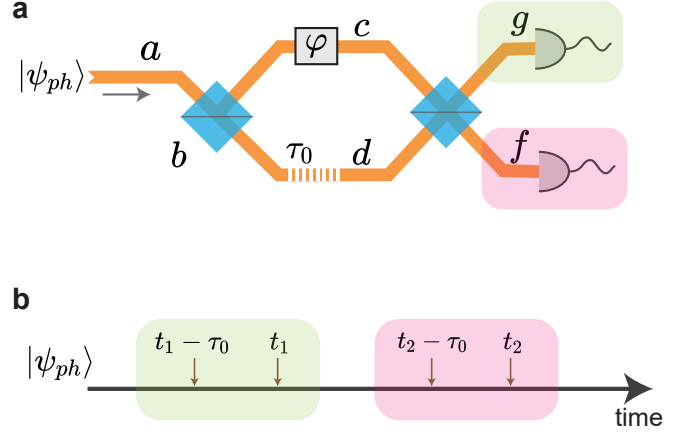
Hong-Ou-Mandel (HOM) interferometry is an indispensable tool for evaluating indistinguishability among photons emitted by a single photon source<sup>7</sup>. As shown in Supplementary Fig. 2a, a typical HOM interferometer consists of an AMZI with a path difference of several nanoseconds and two single photon detectors. The AMZI's differential delay ( $\tau_0$ ) can bring two single photons separated by  $\tau_0$  to temporally overlap for interference. If perfectly indistinguishable, two photons will coalesce and therefore the possibility for registering a photon simultaneously at each detector port is 0. In the HOM second-order correlation measurement, this exhibits as a dip at 0-time delay, i.e.,  $g_{HOM,\parallel}^{(2)}(0) = 0$ . By rotating one photon's polarisation to be perpendicular to the other, the two photons become fully distinguishable and will thus not interfere, resulting  $g_{HOM,\perp}^{(2)}(0) = 0.5$ . Indistinguishability  $M$  is calculated from the correlation values measured 0-delay using

$$M = \frac{g_{HOM,\perp}^{(2)}(0) - g_{HOM,\parallel}^{(2)}(0)}{g_{HOM,\perp}^{(2)}(0)}. \quad (\text{S.8})$$

This methodology applies to an incoherently pumped single photon source, for which the AMZI's delay can easily exceed the photon's coherence and thus ensure the HOM interferometric result does not depend on the AMZI's phase  $\varphi$ .

To apply to a coherently driven light source, the differential delay for the AMZI needs to exceed the coherence time of the driving laser. In our case,  $T_L \sim 100 \mu\text{s}$ . To

produce such amount of delay, tens of kilometers of single mode fibre would be required, which will make the final setup cumbersome and introduce significant loss to the single photon signal. Moreover, a highly asymmetric interferometer can introduce unbalanced chromatic dispersion and thus affect the indistinguishability measurement for broadband single photons.



**Supplementary Fig. 2. HOM interferometry.** **a**, HOM interferometer with a differential delay  $\tau_0$  and a phase delay  $\varphi$ . Its ports are labelled as  $a - g$ . **b**, Due to the presence of AMZI, detector at port  $g$  registers a click at time  $t_1$ , corresponding to two emission times of the light source,  $t_1$  and  $t_1 - \tau_0$ . Similarly, detector at  $f$  port responds at time  $t_2$ , also corresponding to two emission times of the light source,  $t_2$  and  $t_2 - \tau_0$ .

Our HOM interferometer has a delay of  $\tau_0 = 2.1 \text{ ns}$ , which is more than 5 orders magnitude shorter than the laser coherence time. Naturally, its measurement result is phase-dependent. Below we develop a general theory to account for the phase-dependence and thus allow a robust indistinguishability measurement using an AMZI of a short delay.

### A. General description

As shown in Supplementary Fig. 2, a quantum light input  $|\psi_{ph}\rangle$  enters an AMZI through port  $a$  and is split equally into two paths  $c$  and  $d$ . After accumulating a differential delay of  $\tau_0$  and a phase delay of  $\varphi$ , the split signals recombine at the exit 50/50 beam splitter to interfere. Photons exiting from ports  $f$  and  $g$  are detected by two single photon detectors. In the subsequent discussion, we consider only the case that the AMZI having parallel polarisation between its two arms because the result for perpendicular polarisations is trivial.

We consider the light input to have the general form

$$|\psi_{ph}\rangle = \sqrt{p_0}|0\rangle + \sqrt{p_1}|1\rangle + \sqrt{p_2}|2\rangle, \quad (\text{S.9})$$

where  $p_0$ ,  $p_1$  and  $p_2$  represent the probability of 0, 1 and

2 photons at time  $t$ ,  $p_0 + p_1 + p_2 = 1$ , and  $p_2 \ll p_1^2/2$ . The purpose of including the  $|2\rangle$  term is to accurately account for the HOM dip coincidence.

### B. Coincidence probability

A coincidence event with  $f$  detector clicked at  $t_1$  and  $g$  at  $t_2$  involves the input of up to four non-degenerate times,  $t_1$ ,  $t_1 + \tau_0$ ,  $t_2$  and  $t_2 + \tau_0$ , see Supplementary Fig. 2b. Below, we will analyse their coincidence probabilities according to the level of their time degeneracy.

#### 1. Non-degenerate

For intervals  $\Delta t = t_2 - t_1$  that meets both  $|\Delta t \pm \tau_0| \gg T_2$  and  $|\Delta t| \gg T_2$ , there is no degeneracy in the four involved

times and each coincidence therefore is a result of two independent first-order interference events. Consequently, the coincidence probability is simply the product of the count probabilities of individual detectors,

$$\mathcal{C}_0(\varphi) = \mathcal{P}_f \cdot \mathcal{P}_g = \frac{p_1^2}{4} (1 - Mp_0^2 \cos^2 \varphi). \quad (\text{S.10})$$

$\mathcal{C}_0(\varphi)$  forms the coincidence baseline, and depends on the AMZI's phase. At  $\varphi = \pi/2$ , it reaches its maximum.

#### 2. Singly-degenerate: $t_2 - t_1 = \pm \tau_0$

For intervals  $\Delta t = \pm \tau_0$ , two out of the four time slots become degenerate and involve more complicated interference than the baseline case. Rigorously, its coincidence probability can be derived from<sup>3,8</sup>

$$\begin{aligned} \mathcal{C}(\Delta t) &= \langle \psi_{out} | g^\dagger(t + \Delta t) f^\dagger(t) f(t) g(t + \Delta t) | \psi_{out} \rangle \\ &= \langle \psi_{in} | U^\dagger g^\dagger(t + \Delta t) f^\dagger(t) U U^\dagger f(t) g(t + \Delta t) U | \psi_{in} \rangle, \end{aligned} \quad (\text{S.11})$$

where

$$\begin{aligned} U^\dagger f(t) g(t + \Delta t) U &= \frac{c(t - \tau_0)e^{i\varphi} + d(t)}{\sqrt{2}} * \frac{c(t + \Delta t - \tau_0)e^{i\varphi} - d(t + \Delta t)}{\sqrt{2}} \\ &= \frac{1}{4} [a(t + \Delta t - \tau_0)a(t - \tau_0)e^{-i2\varphi} + a(t + \Delta t)a(t - \tau_0)e^{-i\varphi} \\ &\quad - a(t + \Delta t - \tau_0)a(t)e^{-i\varphi} - a(t + \Delta t)a(t)]. \end{aligned} \quad (\text{S.12})$$

For the incident quantum state, since the contribution of multi-photon components is small and has little impact on the final coincidence, we consider only the lowest-order photon state  $|1\rangle$  to capture the main characteristics of the coincidence probability. For  $\Delta t = +\tau_0$ , we can write the operator corresponding based on equation (S.12),

$$\hat{O}_{t,t+\tau_0} = \frac{1}{4} [a(t)a(t - \tau_0)e^{-i2\varphi} + a(t + \tau_0)a(t - \tau_0)e^{-i\varphi} - a(t)a(t)e^{-i\varphi} - a(t + \tau_0)a(t)]. \quad (\text{S.13})$$

In the above equation, we have omitted a term  $-a(t)a(t)e^{-i\varphi}$  because we do not consider multi-photon terms such as  $|2\rangle$  or higher in the incident state. According to the expression of  $\hat{O}_{t,t+\tau_0}$ , the incident state should be the tensor product of three-time quantum states,  $t - \tau_0$ ,  $t$  and  $t + \tau_0$ ,

$$\begin{aligned} \hat{O}_{t,t+\tau_0} |\psi_{t-\tau_0}\rangle |\psi_t\rangle |\psi_{t+\tau_0}\rangle &= \left[ \sqrt{p_0 p_1^2} (e^{-i2\varphi} + e^{-i\varphi} - 1) |000\rangle + \sqrt{p_1^3} e^{-i2\varphi} |001\rangle \right. \\ &\quad \left. \sqrt{p_1^3} e^{-i\varphi} |010\rangle - \sqrt{p_1^3} |100\rangle \right] / 4. \end{aligned} \quad (\text{S.14})$$

Therefore,

$$\mathcal{C}(\tau_0) = \frac{1}{16} p_0 p_1^2 (3 - 2 \cos 2\varphi) + \frac{3}{16} p_1^3. \quad (\text{S.15})$$

For  $\Delta t = -\tau_0$ , one can follow the same derivation process and obtain  $\mathcal{C}(-\tau_0) = \mathcal{C}(+\tau_0)$ . Taking into account of imperfect photon indistinguishability,  $\mathcal{C}(\pm\tau_0)$  is corrected to

$$\mathcal{C}(\pm\tau_0) = \frac{1}{16} p_0 p_1^2 (3 - 2M \cos 2\varphi) + \frac{3}{16} p_1^3. \quad (\text{S.16})$$

### 3. Doubly degenerate: $t_1 = t_2$

At  $\Delta t = 0$ , the four time slots (Supplementary Fig. 2b) become doubly degenerate:  $t_1 = t_2$  and  $t_1 + \tau_0 = t_2 + \tau_0$ . Coincidence at this interval has two contributions: (1) multi-photon components in the input  $|\psi_{ph}\rangle$  and (2) imperfect photon indistinguishability. As these two contributions are on the same magnitude, it is necessary to include the  $|2\rangle$  term in the input in order to derive correctly its coincidence probability. We use  $\psi(t)$  described in equation (S.9) as the input.

Following equation (S.12), the operator for  $\Delta t = 0$  can be written as

$$\hat{O}_{t,t} = \frac{1}{4} [a(t - \tau_0)a(t - \tau_0)e^{-i2\varphi} + a(t)a(t - \tau_0)e^{-i\varphi} - a(t - \tau_0)a(t)e^{-i\varphi} - a(t)a(t)]. \quad (\text{S.17})$$

We only need to consider the states of two time slots, i.e.,  $t$  and  $t - \tau_0$ , leading to

$$\begin{aligned} \hat{O}_{t,t}|\psi_{t-\tau_0}\rangle|\psi_t\rangle = & \left[ \sqrt{2p_0p_2}(e^{-i2\varphi} - 1)|00\rangle + \sqrt{2p_1p_2}e^{-i2\varphi}|01\rangle + \sqrt{2p_1p_2}|10\rangle \right. \\ & \left. + \sqrt{2}e^{-i2\varphi}p_2|02\rangle - \sqrt{2}p_2|20\rangle \right] / 4. \end{aligned} \quad (\text{S.18})$$

Therefore,

$$\mathcal{C}(0) = \frac{1}{2}p_0p_2\sin^2\varphi + \frac{1}{4}p_1p_2 + \frac{1}{4}p_2^2 = \frac{1}{4}(p_2 - p_0p_2\cos 2\varphi). \quad (\text{S.19})$$

At this point, we consider the influence of photon indistinguishability, and  $\mathcal{C}(0)$  should be corrected as

$$\mathcal{C}(0) = \frac{p_2}{4}(1 - p_0M\cos 2\varphi) + \frac{p_1^2 + 4p_1p_2 + 4p_2^2}{8}(1 - M). \quad (\text{S.20})$$

### III. EXPERIMENTAL SETUP

In this section, we provide more information about our experimental setup.

The main experimental apparatus is shown in Supplementary Fig. 3a. We use a 50:50 non-polarising beam splitter (NPBS) to separate the quantum dot (QD) RF signal from a continuous-wave excitation laser (M SQUARED SolsTis PSX XF 5000, with a linewidth of  $\sim 100$  kHz). The RF output is then sent into the measurement apparatuses indicated as panel b, c and d for characterization.

The setup shown in Supplementary Fig. 3b is a standard Hanbury-Brown Twiss setup to measure the auto-correlation function  $g^{(2)}(\Delta t)$  and evaluate the single-photon purity of the input signal. It consists of a 50:50 optical fibre beam splitter and two single photon detectors. A high purity of the incident single-photon state corresponds to a  $g^{(2)}(0)$  value close to 0.

Supplementary Figure 3c illustrates a setup for characterising the first-order correlation function  $g^{(1)}(\tau)$ . In this setup, both beam splitters have a nominal 50:50 reflectance-to-transmittance ratio, and the AMZI's differential delay is 2.1 ns. The count rates at the detectors oscillate with a free-drifting phase  $\varphi$ . By measuring the maximum and minimum values of this oscillation, we can calculate the interference fringe visibility:  $V = |g^{(1)}(\tau_0)|$ . Usually, one detector would suffice. However, the QD blinking effect in our device significantly affects  $g^{(1)}(\tau_0)$

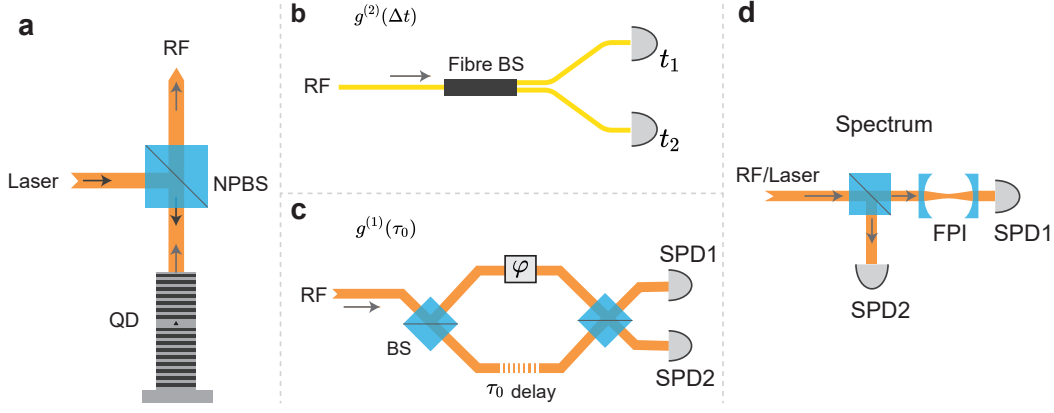
measurement results. Therefore, we use a two-channel summation method to normalise the count rate for visibility calculation. This method effectively eliminates the blinking effect and ensures a reliable measurement of  $g^{(1)}(\tau)$ . The setup in Supplementary Fig. 3c is also used for phase-dependent Hong-Ou-Mandel two-photon interference measurement.

Supplementary Fig. 3d is the setup for measuring the RF frequency spectrum. The RF signal is split into two paths. One path enters the scanning Fabry-Pérot Interferometer (FPI) with a single photon detector (SPD1) recording the signal count rate as a function of the FPI transmission frequency. The other path enters a second single photon detector (SPD2) for normalising SPD1's detection results. The scanning FPI has a free spectral range of 20 GHz and a resolution of 20 MHz.

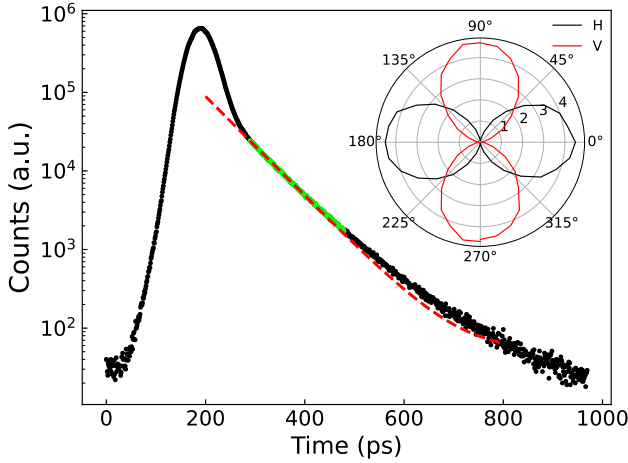
Two superconducting nanowire single photon detectors (SNSPDs) are used for single photon detection. These SNSPDs are characterised to have a single-photon detection efficiency of 78 % and a time jitter of 48 ps at the wavelength of 910 nm. A time-tagger is used for correlation and time-resolved measurements.

### IV. QD-MICROPILLAR DEVICE

Our sample consists of a  $\lambda$ -GaAs layer contain single layer of low-density In(Ga)As QDs sandwiched between two distributed Bragg reflectors formed by 18 (top)



**Supplementary Fig. 3. Experimental setup.** **a**, Coherent single photon source generation device. **b**, Fibre beam splitter for  $g^{(2)}(\Delta t)$  measurement. **c**, Mach-Zehnder interferometer for  $g^{(1)}(\tau_0)$  measurement. **d**, Setup for the spectrum measurement of RF or excitation laser.



**Supplementary Fig. 4. Some important characteristics of the quantum dot single-photon source.** The black dots represent the time evolution of the measured intensity reflected by the device using pulsed excitation. The green dots are extracted to fit the QD exciton lifetime and the red dashed line is the fitted curve, which gives the exciton lifetime of 68.7 ps. The inset shows the count rates (a.u.) as a function of the polarising filter angle at the signal collection port. The black and red curves are two results obtained from QD excited by a continuous 911.55 nm laser with two polarisations parallel to the QD eigen axes.

and 30.5 (bottom) GaAs/Al<sub>0.9</sub>Ga<sub>0.1</sub>As layer pairs. Using scanning reflectance spectroscopy, we determine the resonance of the HE<sub>11</sub> cavity mode to have a central wavelength of 911.55 nm and a linewidth of 0.0975 nm, corresponding to a quality factor (Q) of approximately 9350. At the cavity resonance wavelength, the minimum reflectivity is  $R_{min} = 0.015$ , suggesting an efficient light coupling ( $\sim 98.5\%$ ) into the cavity mode. We acknowledge that this cavity reflectivity is slightly stronger than previously measured<sup>9</sup> using a different experimental setup that

uses a combination of a polarisation beam splitter (PBS) and a quarter wave plate for signal routing. However, the present setup allows free selection of the excitation polarisation.

The QD's neutral exciton transition has a fine-structure splitting of 0.91 GHz. By using polarising filters in the excitation and signal collection paths, we are able to select freely the polarisation of both excitation and signal light and identify the QD's two eigen polarisations (H and V) under resonant condition. The V-exciton is then brought into strict resonance with the cavity through tuning the device temperature to 15.2 K. Aligning the excitation polarisation to one of the QD eigen axes at a time, we are able to measure the polarisation-dependent signal intensity by rotating the polariser at the signal collection path. As shown in the inset of Supplementary Fig. 4, both H and V signals reach a high degree of polarisation extinction ratio of 19.2 dB.

The V-exciton is investigated in all experiments shown in Main Text. Supplementary Fig. 4 shows its time-resolved resonance fluorescence time evolution under 5 ps pulsed excitation using a 80 MHz Ti:S laser. Through the exponential decay, we determine the V-exciton to have a lifetime of 68.7 ps. This lifetime is used to calibrate the incident photon flux  $\bar{n}_{in}$ , i.e., the number of photons per exciton lifetime incident upon the device surface.

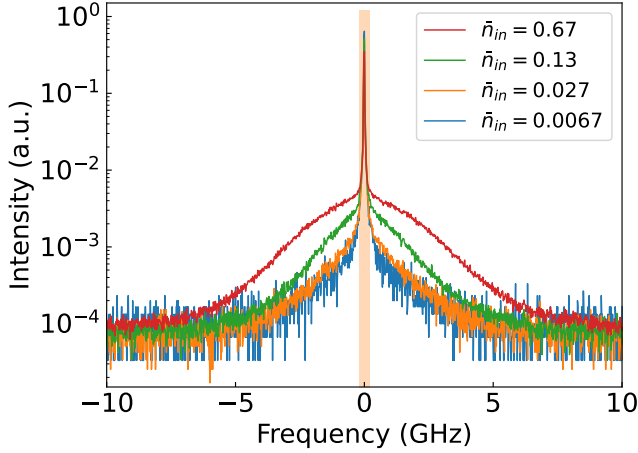
## V. FURTHER EXPERIMENTAL DATA

### A. RF spectra

To accompany Fig. 2, Main Text, we provide several representative RF spectra in Supplementary Fig. 5. At weak excitation limit ( $\bar{n}_{in} \rightarrow 0$ ), the linewidth of the broadband part is determined by the QD transition, and its spectral weight by the finite photon indistinguishability, as evidenced by the almost identical spectra obtained

with  $\bar{n}_{in} \leq 0.027$ . With the increase in the excitation intensity, it is evident that the broadband spectral part grows in both weight and width. This is caused by the increased population of the light-matter excited state, affecting the first-order coherence, see equation (S.1). At these excitation levels, the Rabi splitting or oscillation frequency becomes close to the TLE's radiative linewidth:  $\Omega \sim 1/2\pi T_1$ , and thus affects the overall spectral linewidth. We have previously shown that the broadband part develops into Mollow triplets when  $\bar{n}_{in}$  reaches few-photon level<sup>9</sup>.

Meanwhile, the sharp features in the spectrum, referred to as the coherent part, occupy a decreasing fraction of the total RF, as indicated by the square-shaped orange region. Its fraction is excellently simulated using equation  $I_{coh}/I_{tot} = V_0/(1 + 2\bar{n})$ , as shown in Fig. 2, Main Text as well as in the next Subsection.



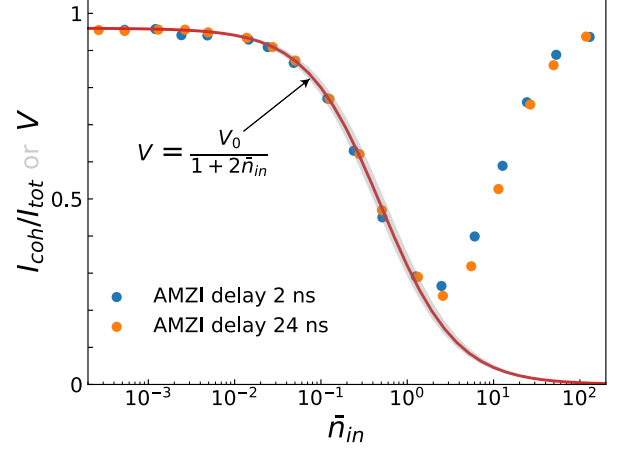
**Supplementary Fig. 5.** RF spectra measured at different excitation intensities.

### B. The first-order coherence visibility data obtained with a polarisation beam splitter setup

The explicit relation  $g^{(1)}(\tau) = 1/(1+2\bar{n})$  (equation (5), Main Text) is one of the key results of the present investigation. To further demonstrate the validity of this explicit result, we supplement the visibility measurement results using a PBS (polarising beam splitter) setup<sup>9</sup> which produces lower laser background. The corresponding  $g^{(2)}(0)$  value at  $\bar{n}_{in} = 0.02$  is 0.0026, which is considerably lower than 0.0040 obtained with the NPBS setup. We measure the first-order interference visibility at different excitation powers with two different AMZI delays of 2 ns and 24 ns, as shown in Supplementary Fig. 6. The two sets of data are approximately identical, because either delay is much less than the laser coherence time  $T_L$ .

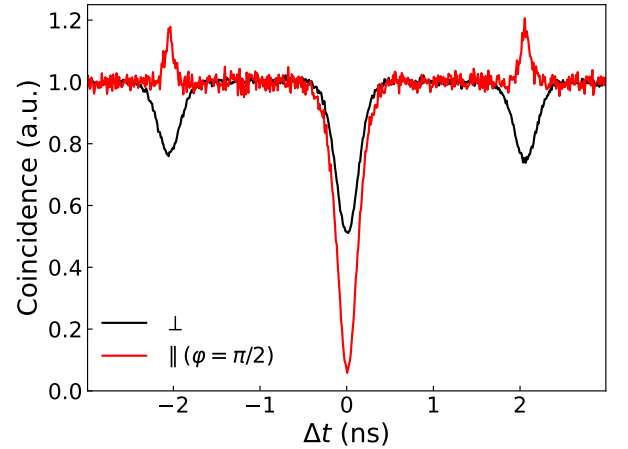
Thanks to the lower laser background, the visibility under weak excitation plateaus at a higher value of 0.96, while the visibility dips deeper down to 0.20 at  $\bar{n}_{in} = 2.5$ ,

than the NPBS data reported in Fig. 2, Main Text. The extended data range allows a more convincing test of our theoretical model. We calculate the theoretical line using  $V = V_0/(1 + 2\bar{n}_{in})$  with  $V_0 = 0.96$ , which exhibits an almost perfect match to the experimental data sets.



**Supplementary Fig. 6.** The first-order interference visibility obtained from a PBS setup. Two AMZIs of 2 ns and 24 ns were used in this experiment. The solid line in the figure corresponds to the calculation using  $V = V_0/(1 + 2\bar{n}_{in})$  with  $V_0 = 0.96$ . The upper and lower boundaries of the grey shaded region are  $V_0/(1 + x\bar{n}_{in})$ , where  $x = 2(1 \pm 0.15)$ , highlighting the tight fit of our model.

### C. Indistinguishability measurement for a coherently driven source



**Supplementary Fig. 7.** Phase-sensitive HOM measurement. Interfering coincidence of two photon beams with perpendicular/parallel polarisations. For the results of parallel polarisations, the phase range of the HOM AMZI is post-selected in the range between  $9\pi/20$  and  $\pi/2$ . The excitation intensity  $\bar{n}_{in}$  is 0.0067.

For a coherently driven source, both the baseline and 0-delay coincidences are phase dependent, see equations (Eqs. S.10) and (S.20). However, at  $\varphi = \pi/2$ , both reach their respective maxima. Importantly at this phase delay, the baseline coincidence becomes identical to the case when the polarisations of two HOM arms are set orthogonal to each other. Consequently, we can calculate the indistinguishability using

$$M = \frac{\mathcal{C}_{ref}^{\perp}(0) - \mathcal{C}_{\pi/2}^{\parallel}(0)}{\mathcal{C}_{ref}^{\perp}(0)}, \quad (\text{S.21})$$

where  $\mathcal{C}_{ref}^{\perp}(0)$  is the 0-delay coincidence for orthogonal polarisations and  $\mathcal{C}_{\pi/2}^{\parallel}(0)$  the 0-delay coincidence for parallel polarisations with the AMZI's phase set to  $\pi/2$ .

We apply this new method to our RF source and obtain  $M = 0.886$  at an excitation intensity of  $\bar{n}_{in} = 0.0067$ , as shown in Supplementary Fig. 7.

- 
1. Steck, D. A. Quantum and atom optics. <http://steck.us/teaching> (revision 0.14, 23 August 2023).
  2. Tomm, N. *et al.* A bright and fast source of coherent single photons. *Nat. Nanotech.* **16**, 399–403 (2021).
  3. Lored, J. *et al.* Generation of non-classical light in a photon-number superposition. *Nat. Photon.* **13**, 803–808 (2019).
  4. Phillips, C. L. *et al.* Photon statistics of filtered resonance fluorescence. *Phys. Rev. Lett.* **125**, 043603 (2020).
  5. Hanschke, L. *et al.* Origin of antibunching in resonance fluorescence. *Phys. Rev. Lett.* **125**, 170402 (2020).
  6. Masters, L. *et al.* On the simultaneous scattering of two photons by a single two-level atom. *Nat. Photon.* **17**, 972–976 (2023).
  7. Santori, C., Fattal, D., Vučković, J. & Yamamoto, Y. Indistinguishable photons from a single-photon device. *Nature* **419**, 594 – 597 (2002).
  8. Legero, T., Wilk, T., Kuhn, A. & Rempe, G. Time-resolved two-photon quantum interference. *Appl. Phys. B* **77**, 797–802 (2003).
  9. Wu, B. *et al.* Mollow triplets under few-photon excitation. *Optica* **10**, 1118 – 1123 (2023).